JOURNAL OF MATERIALS SCIENCE **39** (2004) 1153–1168

Review
Observations of common microstructural issues associated with dynamic deformation phenomena: Twins, microbands, grain size effects, shear bands, and dynamic recrystallization

L. E. MURR, E. V. ESQUIVEL
Department of Metallurgical and Materials Engineering, The University of Texas at El Paso, El Paso, TX 79968, USA
E-mail: fekberg@utep.edu

Plane-wave shock deformation has been shown to produce deformation twins or twin-faults in essentially all metal and alloys. In FCC metals and alloys twinning depends upon stacking-fault free energy (SFE) and a critical twinning pressure; which increases with increasing SFE. For impact cratering where the shock wave is spherical and a prominent deviatoric (shear) stress is involved, metals and alloys with high SFE form microbands coincident with {111} plane traces while low SFE metals and alloys either form mixtures of twins and microbands or microtwins. Oblique shock loading of copper also produces mixtures of twins and microbands. Both microtwins and microbands increase in volume fraction with increasing grain size. BCC iron is observed to twin in both shock loading and as a result of impact cratering. Impact craters, shaped charges, and other examples of extreme deformation and flow at high strain rates exhibit various regimes of shear bands and dynamic recrystallization as a mechanism for solid-state flow. Deformation twins and microbands are also often precursors to this process as well. Examples of these phenomena in FCC materials such as Al, Ni, Cu, stainless steel and brass, and BCC materials such as Fe, W, Mo, W-Ta, and Ta are presented; with emphasis on optical metallography and transmission electron microscopy.

1. Introduction

Beginning with the classic work of Rinehart and Pearson [1] Rice *et al*. [2], and Smith [3], and the early summary of the response of metals and alloys to high-velocity and shock deformation [4], interest has grown in dynamic deformation phenomena. The role that dislocations play in these phenomena was recognized early by Armstrong [5] and others [3, 6] along with effects of grain size in polycrystalline metals [7, 8], especially Armco iron [7], where lower shock pressures were observed for the occurrence of twinning in larger grain sizes. It is now well known that increasing grain size in metals and alloys decreases the twinning threshold stress and increases the propensity for deformation twins, especially for plane-wave shock and related high-strain-rate phenomena [7–11]. Correspondingly, twinning threshold stresses decline with increasing temperature and strain rates, and twinning and slip become competitive processes which characterize a slip-twinning transition. For a specific grain size, the slip-twinning transition varies with temperature and strain rate. Armstrong and Worthington [12] earlier recognized two important effects: the necessity of microslip for twin initiation and the large grain-size dependence of the twinning stress.

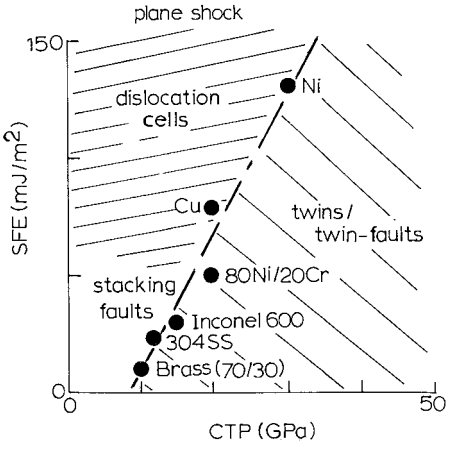

Figure 1 Stacking-fault free energy (SFE) versus critical twinning pressure (CTP) for some fcc metals and alloys. (After Murr [13]).

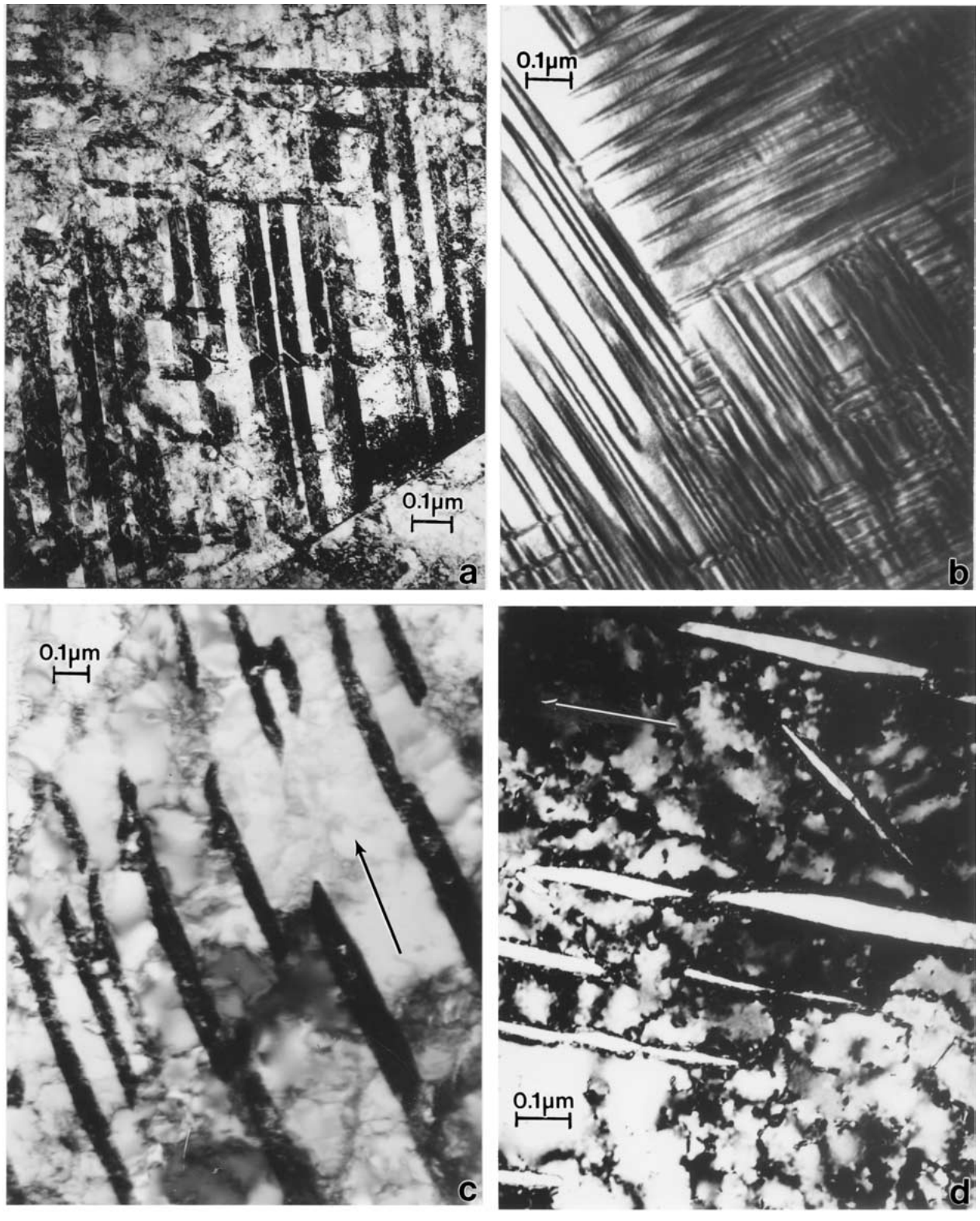

Figure 2 Plane shock-induced microtwins in materials. (a) FCC Ni; 30 GPa, 2 μs pulse duration. (b) $YBa_2Cu_3O_7$ superconductor; 19 GPa. (c) Bcc Ta; 45 Gpa, 2 μs pulse duration. (d) Bcc Mo; 35 GPa, 2 μs. All orientations (001). Arrows in (c) and (d) denote common [$0\bar{2}4$] directions coincident with the traces of (121) twin plane.

For plane-wave shock loading of metals and alloys there is, as a consequence of the threshold twinning stress, a critical twinning pressure (CTP) below which deformation twins do not occur for a specific grain size or grain-size range. In the case of fcc metals and alloys, the CTP varies with stacking-fault free energy (SFE); increasing with decreasing SFE [13]. Furthermore, DeAngelis and Cohen [14] found an orientation dependence for the twinning threshold stress or CTP: for Cu single crystals the requisite pressure for twinning in [001] was 14 GPa while for [111] twinning it was 20 GPa. Meyers and Murr [15] have reviewed these and other effects on deformation twinning, including shock pulse duration and the initial microstructure of metals and alloys. Similar to the effects of very small grain sizes, very dense microstructures also limit or prevent deformation twins from forming during plane-wave shock loading.

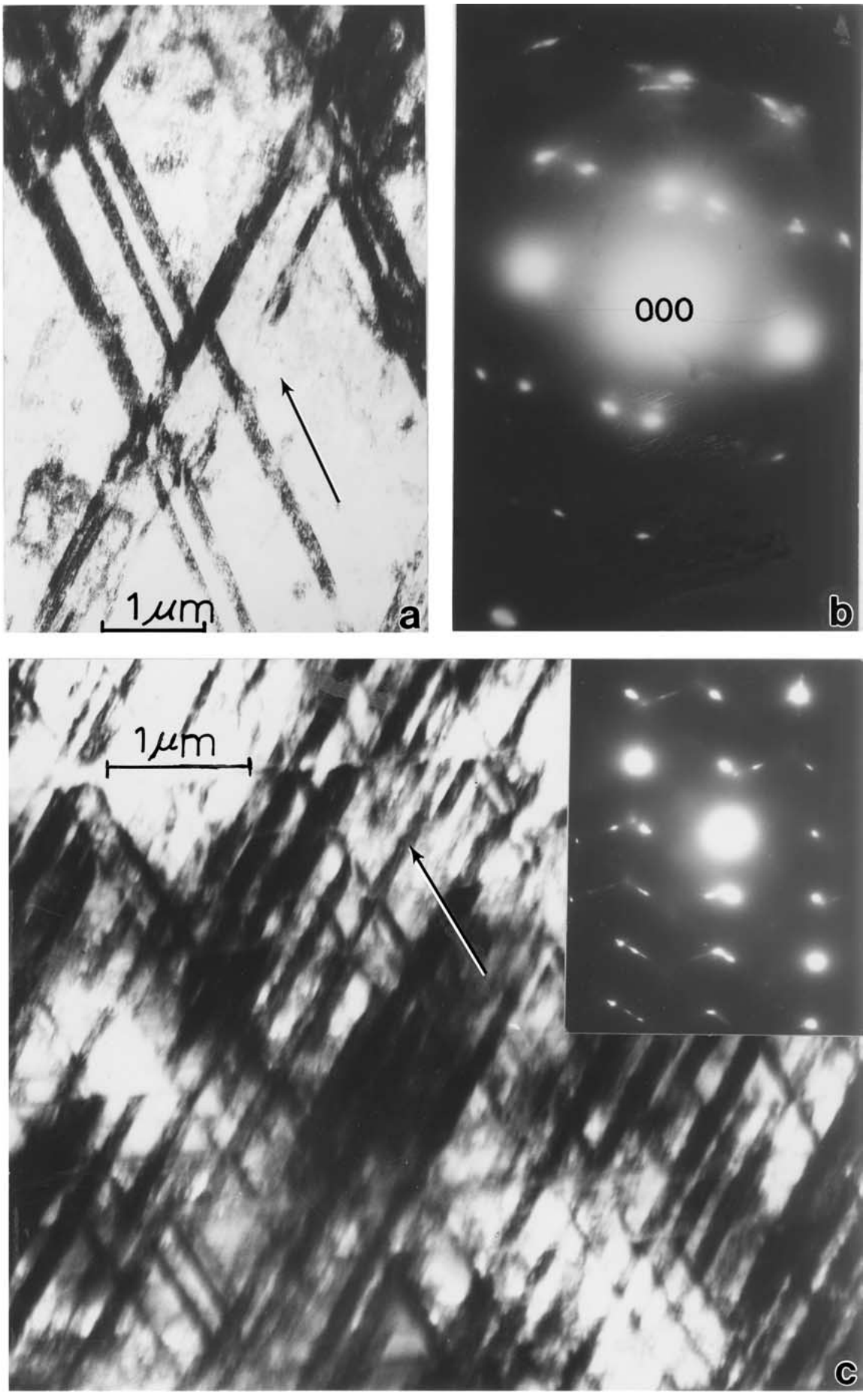

Figure 3 Plane shock-induced microtwins in brass (70 Cu-30 Zn) (a) and 304 stainless steel (b). The shock pressure in (a) and (b) was 35 GPa; 2 μs pulse duration. (112) orientations; arrows indicate $[13\bar{2}]$ directions coincident with traces of $(\bar{1}11)$ planes at $\sim 62^\circ$ with the grain surface. Twin reflections are prominent in the SAED pattern inserts in (a) and (b).

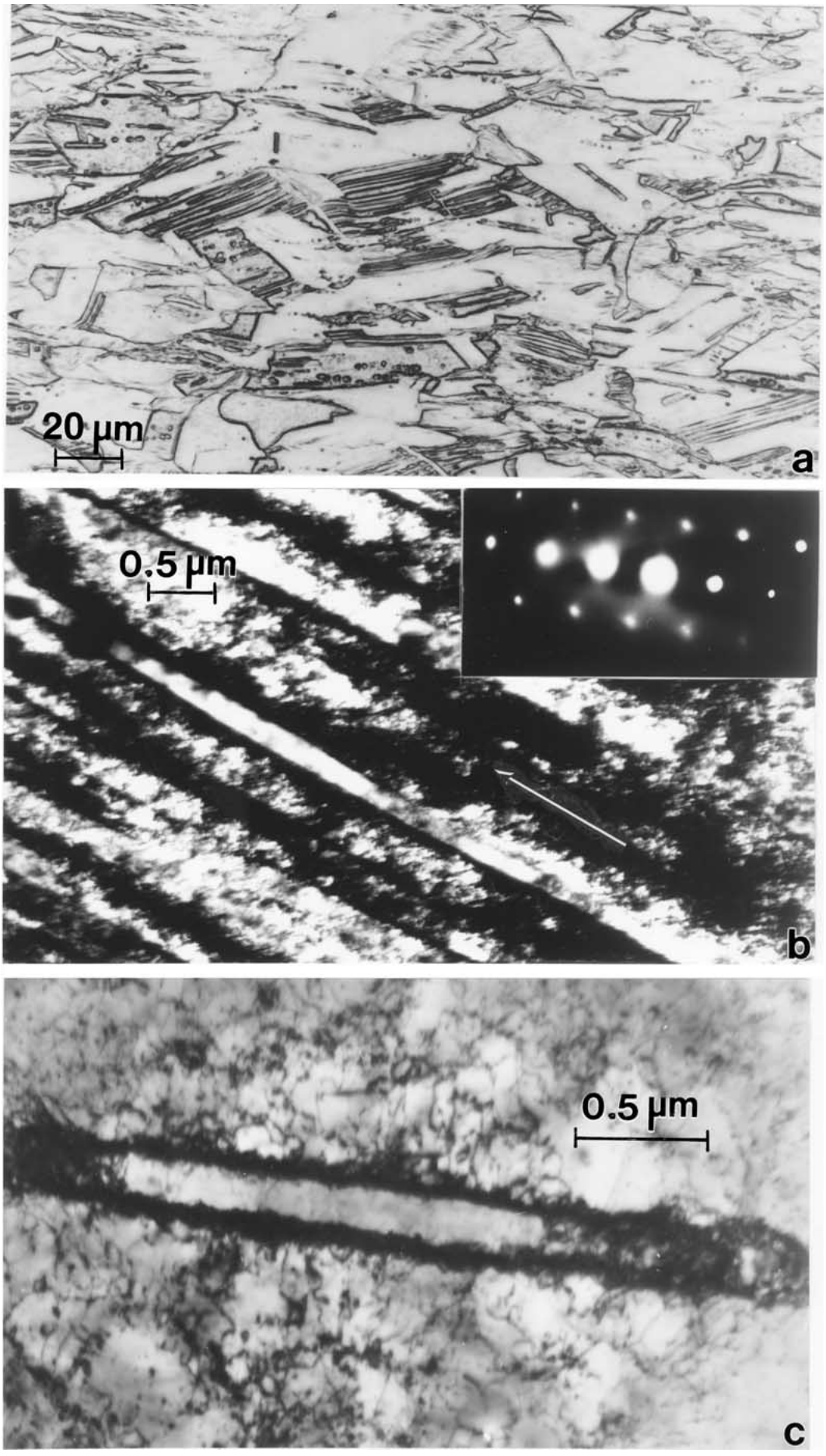

Figure 4 Crater-related microstructures in impacted copper target (~6 km/s impact velocity for aluminum projectile). (a) Optical microscope image several millimeters below the crater bottom showing linear defects. (b) TEM image showing microbands coincident with [1$\bar{1}$2] (arrow). SAED pattern shows [110] zone with no twin reflections (at <111>/3). Arrow in pattern shows ~2° misorientation. (c) TEM image of isolated microband showing heavy dislocation wall structure.

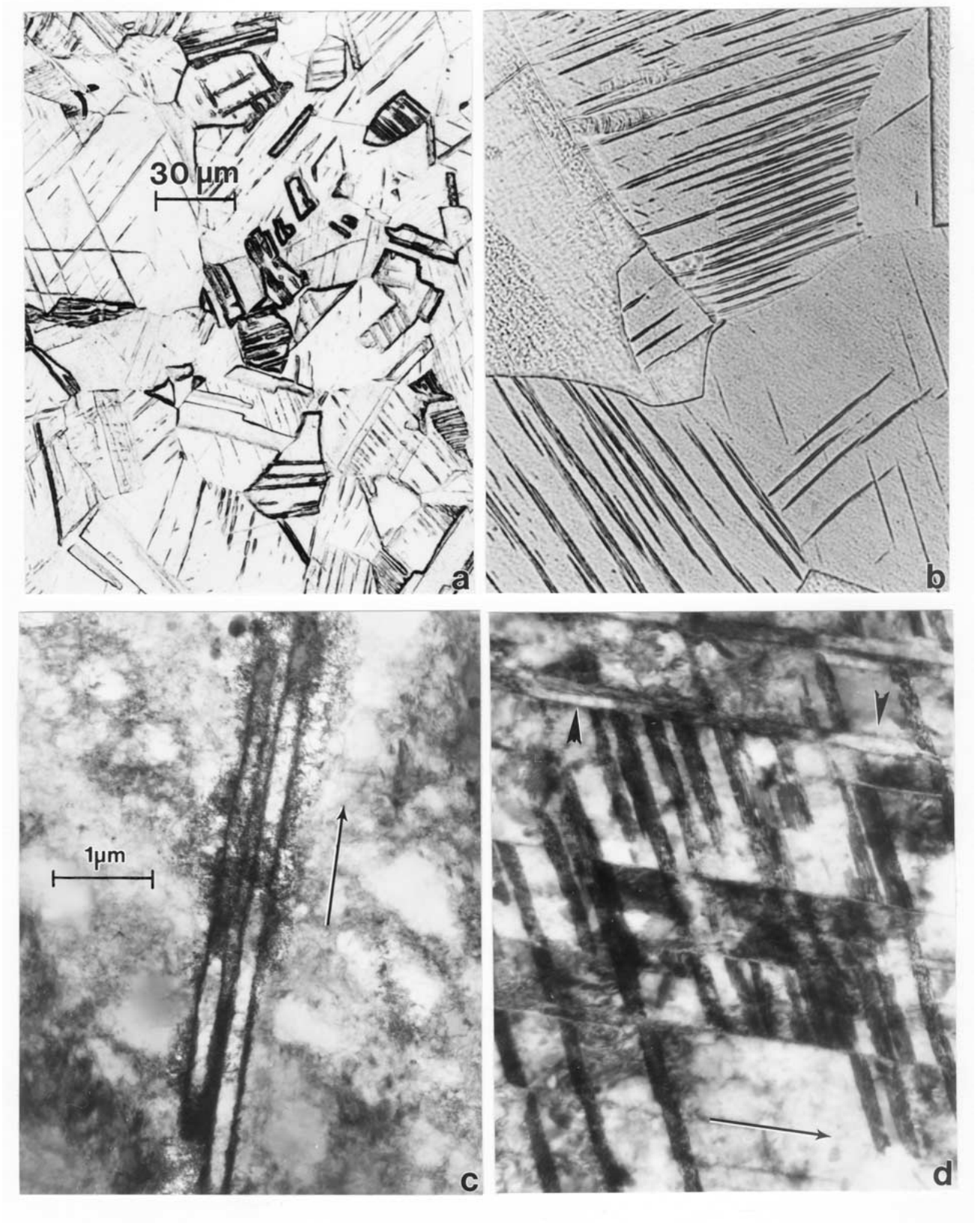

Figure 5 Intermixed microtwins and microbands in oblique shock-loaded copper. (a) and (b) show two different grain sizes (141 and 375 μm respectively) where there is an increase in linear defects with increasing grain size ((a) to (b)). (c) Two isolated microbands coincident with [1$\bar{1}$2] (arrow) in (110) orientation. (d) Intermixed microtwins and microbands (M) oriented as in (c). Magnification of (b) is the same as shown in (a). Magnification of (c) and (d) is the same as indicated in (c).

Recently, Quinones *et al*. [16, 17] observed that the microstructure created below impact craters in polycrystalline copper contained no deformation twins or twin-faults; however microbands coincident with the {111} slip planes or their trace directions were observed at impact conditions which produced peak shock pressures many times the critical twinning pressure for copper [13]. Huang and Gray [18] have described microbands in quasi-statically deformed materials, including shock loaded and deformed copper, but the

microtwin-microband transition mechanism remains unclear. Sanchez *et al*. [19] have examined the microstructures in obliquely shock loaded copper rods and found mixtures of microbands and microtwins; and more recent studies of impact crater behavior in stainless steel indicated a roughly 1 in 10 ratio of microbands to microtwins, suggesting that stacking-fault free energy may play a role.

Deformation twins have also been shown to coincide with and to act as precursors to flow features characterized by wide, overlapping shear bands composed of dynamically recrystallized (DRX) and dynamically recovered (DRV) grain structures in W columnar-grained rod penetrators [20]. Deformation twins have been observed in association with DRX microstructures in an iron explosively-formed penetrator (EFP) [21]. DRX microstructures and overlapping shear bands have also been observed to accommodate the extreme flow of shaped charge jets [22, 23] and crater formation and rim jetting associated with high velocity and hypervelocity impact cratering in metal targets [16, 17, 24].

This paper has several objectives. First, it seeks to examine issues such as the slip-twinning transition and the role played by grain size and stacking-fault free energy, especially in dynamic deformation of fcc metals and alloys. Second, examples of plane-wave-shock-produced deformation twin-faults will be briefly reviewed in both fcc and bcc metals and alloys in order to provide a basis for comparison with microbands associated with high velocity impact craters. Preliminary results for nickel and 304 stainless steel craters will be presented because they represent extremes in SFE (130 mJ/m^2 versus 20 mJ/m^2 respectively [25]). Finally, the role of DRX and DRV in facilitating solid-state flow in shaped charge jet extension, crater formation, and rod penetration into metal targets will be illustrated with examples involving bcc Fe, fcc Cu, and bcc W-4% Ta. This paper will emphasize and compare microstructures (deformation twin-faults or microtwins, microbands, and DRX) observed by transmission electron microscopy (TEM).

2. Experimental issues

The details for plane-wave shock loading of numerous metal and alloy specimens have been reviewed by Murr [26]. Techniques for the collection and analysis of shaped charge fragments have also been described in detail [27, 28] as have techniques for examining microstructures associated with impact craters [16, 17, 29–31] and the penetration of thick targets by long, dense rods [32, 33]; including the metallography (both optical and electron) of penetrator rods themselves [20, 34, 35].

This paper will emphasize both optical metallography (OM) and transmission electron microscopy (TEM) of microstructures associated with the dynamic deformation phenomena alluded to above; especially microtwins in plane-wave shock deformation, microbands in impact craters, and dynamic recrystallization-related microstructures involved in adiabatic shear bands and characteristic solid-state flow phenomena. The corresponding etchants for observing microstructures by optical metallography as well as by TEM have been described in detail elsewhere. These will include the following fcc metals and alloys: Cu [17], Ni [36], aluminum alloy 6061 [37], 304 stainless steel [38, 39] and brass (70 Cu = 30 Zn) [38]. The following bcc metals and alloys will include Fe, [40] Mo [8], Ta [41], and W-Ta [35]. The TEM analysis has involved conventional TEM utilizing a 200 kV operating potential, and a goniometer-tilt stage.

3. Results and discussion

3.1. Deformation microtwins in plane-wave shock-loaded metals and alloys

Fig. 1 reproduces the critical twinning pressure (CTP) versus the room-temperature-corrected stacking-fault free energy (SFE) [25] data [13] for a number of fcc metals and alloys. Figs 2 and 3 illustrate a few examples of shock-induced microtwins characteristic of this data and some additional systems. Fig. 2 compares microtwins in fcc Ni (Fig. 2a), $YBa_2Cu_3O_7$ superconductor (having an orthorhombi crystal structure with $|\mathbf{a}| = 3.83$ Å, $|\mathbf{b}| = 3.87$ Å, and $|\mathbf{c}| = 11.7$ Å) (Fig. 2b), bcc Ta (Fig. 2c), and bcc Mo (Fig. 2d). The corresponding grain sizes in Fig. 2 were 35, 75, 43, and 67 μm in (a) to (d) respectively. Correspondingly Fig. 3 compares fcc brass (70 Cu-30 Zn) (Fig. 3a) and fcc 304 stainless steel (Fig. 3b); with grain sizes of 120 and 21 μm respectively. The selected-area electron diffraction (SAED) pattern inserts in Fig. 3 show prominent twin reflections for twins in intersecting ⟨132⟩ trace directions corresponding to twins or twin-faults in {111} planes inclined ∼62° with the (112) grain surface. It can be noted in Fig. 3b that there is no apparent α'-martensite formation at twin-fault intersections which has been observed for high-strain uniaxial and biaxial deformation of 304 stainless steel [42, 43].

It is notable on comparing deformation microtwins in fcc metals and alloys that they exhibit fairly regular shapes with their edges parallel to the {111} trace directions (arrows in Figs 2a and 3), while bcc microtwins can exhibit similar features (Fig. 2c as well as irregular, lenticular shapes (Fig. 2d) but generally aligned with the traces of {112} planes (arrows in Fig. 2c and d). The example of twinning in shock loaded, superconducting $YBa_2Cu_3O_7$ exhibits other lenticular-like shapes for microtwins coincident with {110} planes.

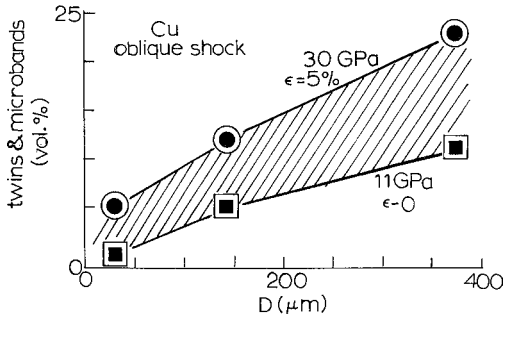

Figure 6 Microtwins (solid) and microbands (open) versus grain size (D) for oblique shock-loaded copper as in Fig. 5 at peak pressures and corresponding residual strains (ε) shown. Data from [19].

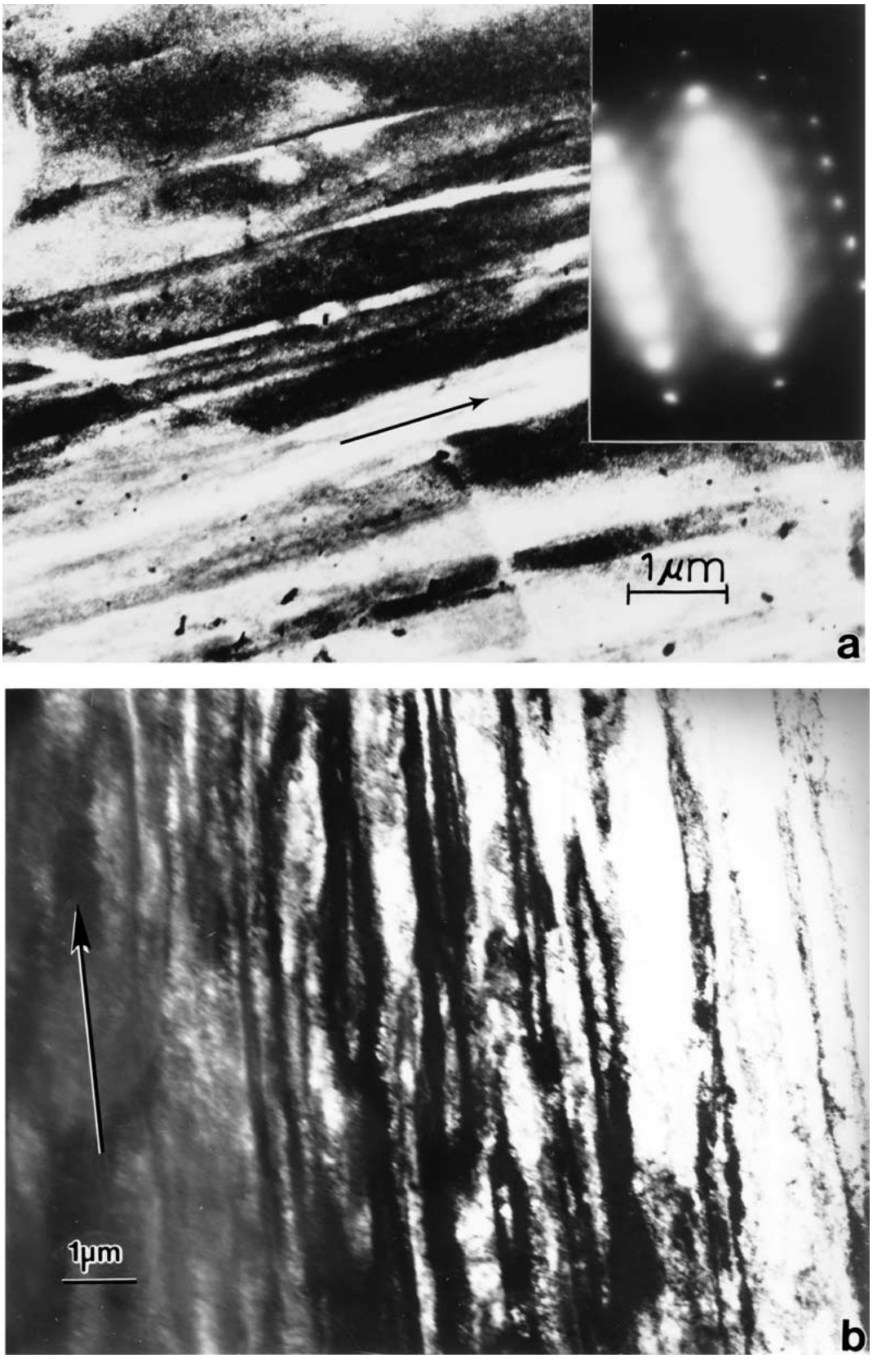

Figure 7 Microbands associated with impact craters in 6061 aluminum alloy (a) and nickel (b). The orientation in (a) and (b) is (110) and the arrows indicate the $[1\bar{1}2]$ direction coincident with traces of $(1\bar{1}\bar{1})$ planes at 90° to the grain surface. Note slight arcing of spots in SAED pattern inserts indicative of very small (∼2°) misorientations. Magnification is the same and shown in (a).

Dislocation mechanisms describing deformation twin formation in fcc and bcc materials in particular have been developed by Cohen and Weertman [44] and Sleeswyk [45] respectively, and involve systematic or unsystematic dislocation glide on the respective twin planes: {111} for fcc and {112} for bcc; with corresponding dislocation Burgers vectors in ⟨112⟩ and ⟨111⟩ directions for fcc and bcc metals and alloys respectively. The unsystematic {111} glide of a <112>/6 partial dislocations in plane-wave shock-loaded fcc

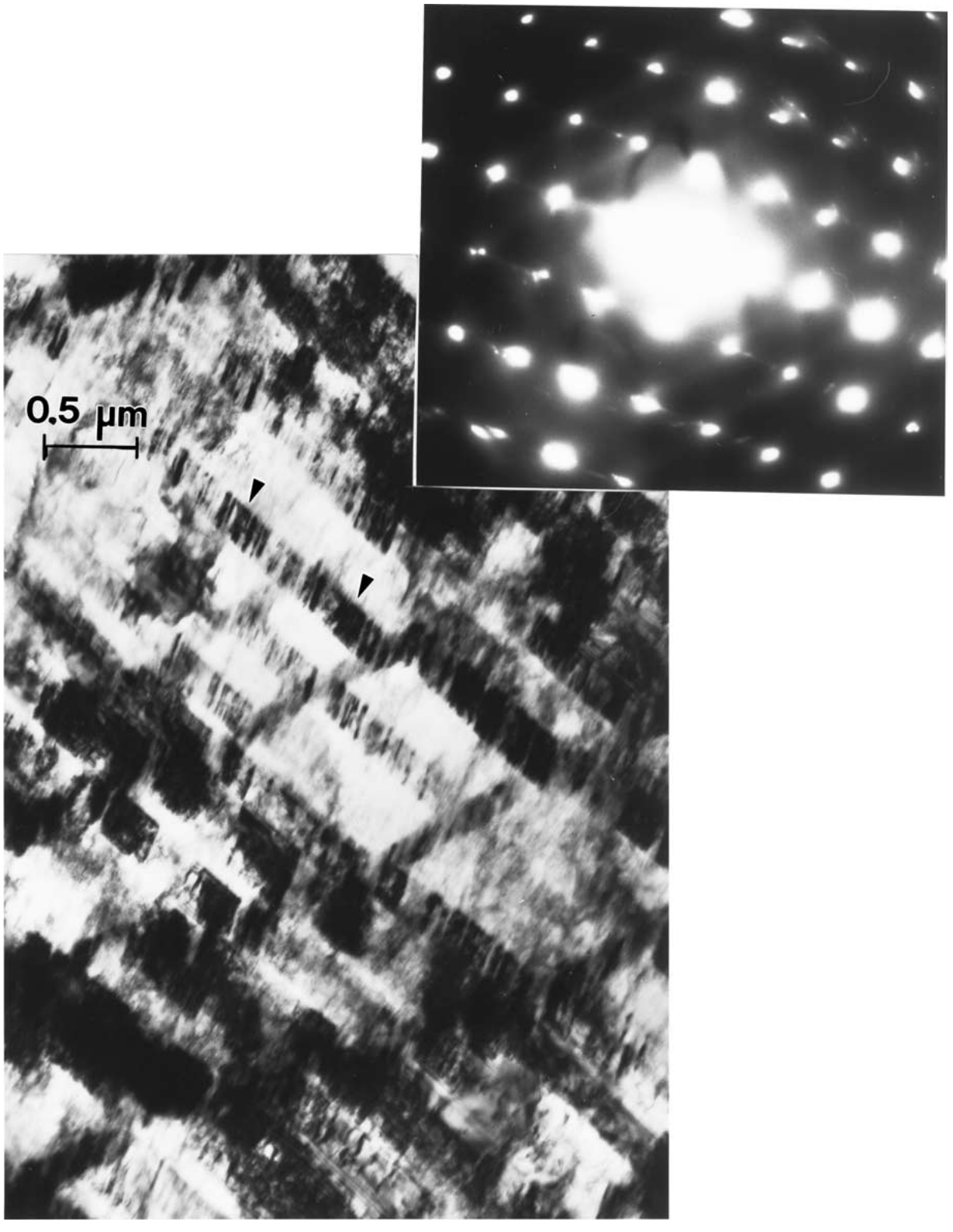

Figure 8 Microtwins and α'-martensite at their intersections in 304 stainless steel impact crater region (3.4 km/s impact of steel projectile). α'-martensite is indicated at arrows.

materials produces the so-called twin-fault, microtwin structures consisting of intermittent thin twin segments interrupted by irregular layers of intrinsic stacking faults.

The partitioning of individual grains which occurs with the development and propensity of microtwins contributes to hardness and yield stress increases. Within a range of peak shock pressures from the CTP (Fig. 1), the hardness of shocked metals and alloys increases with increasing pressure [15, 26] up to some saturation pressure.

3.2. Microbands and microtwins in non-planar-shock-loaded/impacted metals and alloys

Fig. 4 illustrates the microstructures associated with impact craters in copper targets where the corresponding

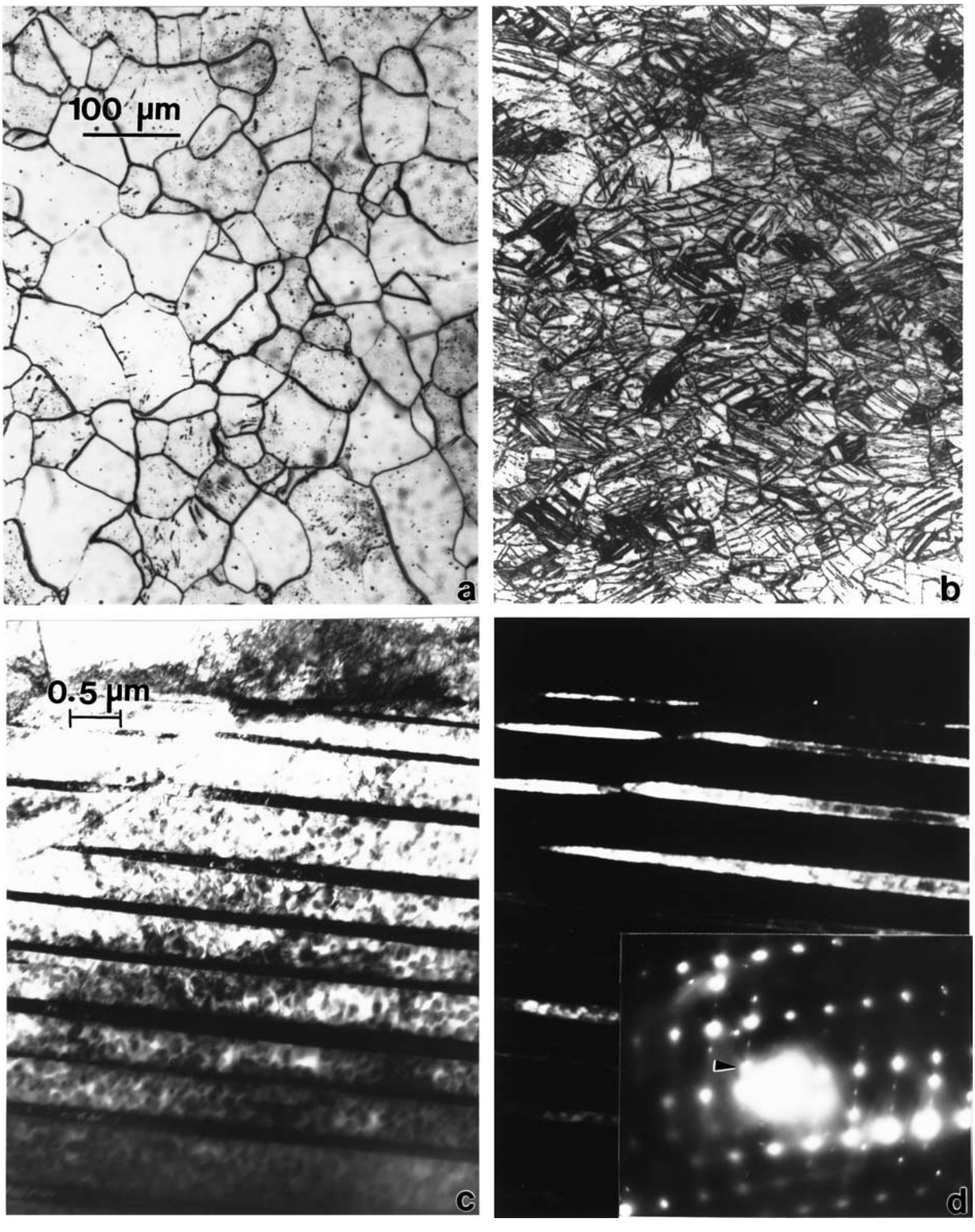

Figure 9 Deformation microtwins associated with impact crater in iron target impacted by steel projectile at 3.3 km/s. (a) Starting grain structure of iron target. (b) Microtwins (Neumann bands). (c) TEM bright-field image of twins in (311) orientation. (d) TEM dark-field image using a <112>/3 twin reflection marked with arrows in SAED pattern insert. Magnification is the same in (a) and (b); as shown in (a). Magnification of (d) is the same as shown in (c).

impact pressure (Hugoniot shock pressure) exceeds the CTP for plane shock loading. While the general appearance from OM (Fig. 4a) would indicate twinning, the TEM images in Fig. 4b and c are clearly indicative of {111} microbands which have been observed previously in some shock loaded and quasi-statically deformed Cu and other metals [46–48], and described in considerable detail by Huang and Gray [18]. It can be noted from Fig. 4b that the microbands are not as regular as microtwins but are nonetheless coincident with the traces of {111} planes. The microband widths (Fig. 4b and c) are between about 0.2 and 0.3 μm and are only slightly misoriented ($\sim$2–3°) relative to the matrix (Fig. 4b SAED pattern insert). Correspondingly,

twin widths in plane-wave shock loaded Cu are similar to those for Ni as shown at intersections of microtwins in Fig. 2a to be around 0.02 μm. Moreover the microband interface is a dislocation double wall [18] which does not necessarily extend continuously over a {111} plane and therefore does not always provide a planar projection in TEM images as implicit in Figs 2a and 3.

These variations in microtwins and microbands in Cu as well as their similarities, especially when viewed in etched surfaces by optical metallography, are illustrated in Fig. 5 which also illustrates the increasing propensity for both microbands and microtwins with increasing grain size on comparing Fig. 5a and b. It is difficult to distinguish microtwins and microbands in the obliquely shock-loaded Cu bar samples illustrated in Fig. 5a and b. However they are clearly recognizable even on comparing the bright-field TEM images in Fig. 5c and d. Note that the surface orientations in both Fig. 5c and d are identical and the arrows indicate traces of {111} planes along [112] at 90° to the $(1\bar{1}0)$ grain surface.

Fig. 6 presents a more quantitative analysis for the variation of microtwins and microbands for the oblique shock loading of Cu rods at the corresponding pressures shown. The shading in Fig. 6 represents a rough mix of both microtwin and microband volume fractions or relative frequency of occurrence. Note that the corresponding minimum pressure (11 GPa) is below the average CTP (~20 GPa) for plane-wave shock loading (Fig. 1).

In a recent comparison of microstructures associated with Fe and 304 stainless steel impact craters [39] microtwins were observed to occur roughly 10 times more frequently than microbands and in contrast to Cu (Fig. 4), the implications are that SFE has a recognizable effect as originally suggested for microband production by Jackson [48]. Figs 7 and 8 provide some additional evidence for SFE influence. In Fig. 7a, only microbands are observed for impact crater-related deformation in a 6061-aluminum alloy target; impacted at 5.45 km/s with a glass projectile. Considering that this alloy contains roughly 4% Cu and that the room temperature (25°C) SFE values for pure Cu and Al are 80 mJ/m^2 and 160 mJ/m^2 respectively [25] the room temperature estimate for the 6061 aluminum alloy is 150 mJ/m^2. However, although Al 6061 may have a relatively high SFE, Gray and Follansbee [49] observed some microbands intermixed with twins in Al 6061-T6 plane-wave shock loaded at 13 GPa. These effects may be due in part to the dense, starting dislocation microstructures after the T6 heat treatment.

In Fig. 7b, microbands typical of the microstructure associated with impact crater formation in Ni targets impacted with steel projectile at 3.4 km/s can be contrasted with plane-wave-shock-loading-induced microtwins in Ni as shown typically in Fig. 2a. The corresponding room temperature SFE for Ni is roughly 130 mJ/m^2. Consequently, for metals and alloys with SFE above about 80 mJ/m^2 (Cu, Ni, and 6061-Al), microbands are formed in the microstructure of impact craters in contrast to microtwins in plane-wave shock loaded microstructures; particularly where there is essentially no residual, compressive strain ($\varepsilon_z \cong 0$).

In contrast to Cu, Ni, and 6061-Al alloy, the microstructure associated with impact craters in 304 stainless steel (SFE ~ 20 mJ/m^2) is dominated by microtwins [39]. In addition, as illustrated in Fig. 8, α'-martensite is observed at the microtwin intersections which is uncharacteristic of plane-wave shock loading; as illustrated typically in Fig. 3b; although small amounts of α'-martensite have been observed at shock pressures as low as 15 GPa near liquid nitrogen temperature [50]. Considerably more α'-martensite forms when a uniaxial or biaxial strain is imposed. Consequently strain, strain-rate, and stress geometry are important features in α'-martensite formation.

As originally discussed by Armstrong and Zerilli [51], iron has a particularly low twinning threshold at high strain rate, and Foley and Howell [52] observed profuse twinning (Neumann bands) nearly 80 years ago in plane-impacted iron even at low impact velocities. More recently Murr *et al*. [39, 40] observed profuse microtwins associated with iron impact craters at projectile velocities of only 0.5 km/s; corresponding to a peak, instantaneous shock pressure of only 7 GPa for impacting steel projectiles. These features are illustrated in Fig. 9. It is interesting to compare Fig. 9b with Fig. 5a for example. While Thuillier and Rauch [53] have observed microband formation in quasi-statically deformed, bcc mild steel, there are no microbands in

METAL OR ALLOY	SFE (mJ/m²)	PLANE SHOCK MICROSTRUCTURE	IMPACT CRATER (SPHERICAL SHOCK) MICROSTRUCTURE
Al 6061	150	microtwins*	microbands
Ni	130	microtwins	microbands
Cu	80	microtwins	microbands
304 Stainless	20	microtwins	microtwins†
brass (70 Cu-30 Zn)	10	microtwins	microtwins

*Some observations of intermixed microbands in heavily-deformed starting material.
†Some intermixed microbands (approximately 1 in 10 microtwins)

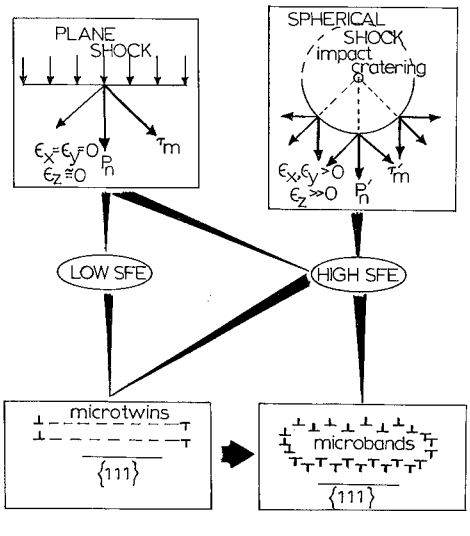

Figure 10 Matrix and schematic for the microtwin-microband transition in fcc metals and alloys deformed in planar shock and impact cratering. Arrows indicate the path sequences. P_n, P'_n and T_m, T'_m are the normal (shock) stress and deviatoric stresses respectively. Strains are denoted ε.

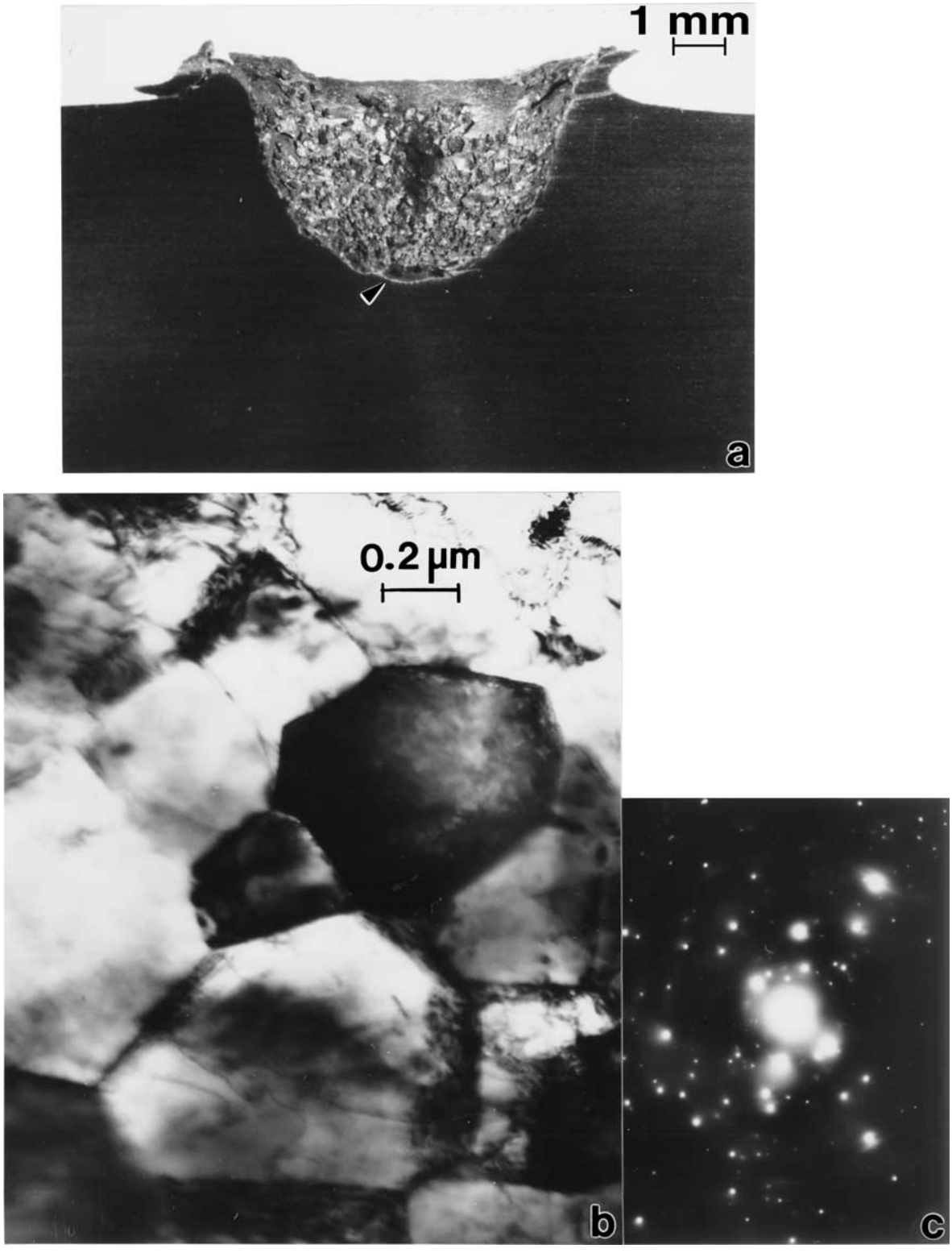

Figure 11 Impact crater in iron target (3.3 km/s steel projectile) (same as Fig. 9b–d). (a) Arrow marks narrow (∼100 μm) zone at crater wall composed of dynamic recrystallization regime shown in TEM image in (b). (c) Shows SAED pattern for (b).

the crater-related microstructures illustrated in Fig. 9 for Fe.

Recent observations of residual microstructures associated with impact craters in 70 Cu - 30 Zn (cartridge brass) [54] show only microtwins similar to those for plane-wave shock loaded brass in Fig. 3a. Taken together with the observations of impact crater-related microbands in Al 6061 and Ni in Fig. 7a and b respectively, and microtwins and α'-martensite formation shown in Fig. 8 for 304 stainless steel, there emerges a compelling sense of the role of SFE and the mode of deformation (planar shock versus impact-related spherical shock) in the microtwin-microband transition. Fig. 10 provides a summary of these effects and some simple graphics illustrating the specific path sequences for microtwin and microband formation in dynamically deformed fcc metals and alloys. The actual dislocation mechanisms differentiating microtwin versus microband formation in Fig. 10 could involve those represented in an earlier cross-slip-related

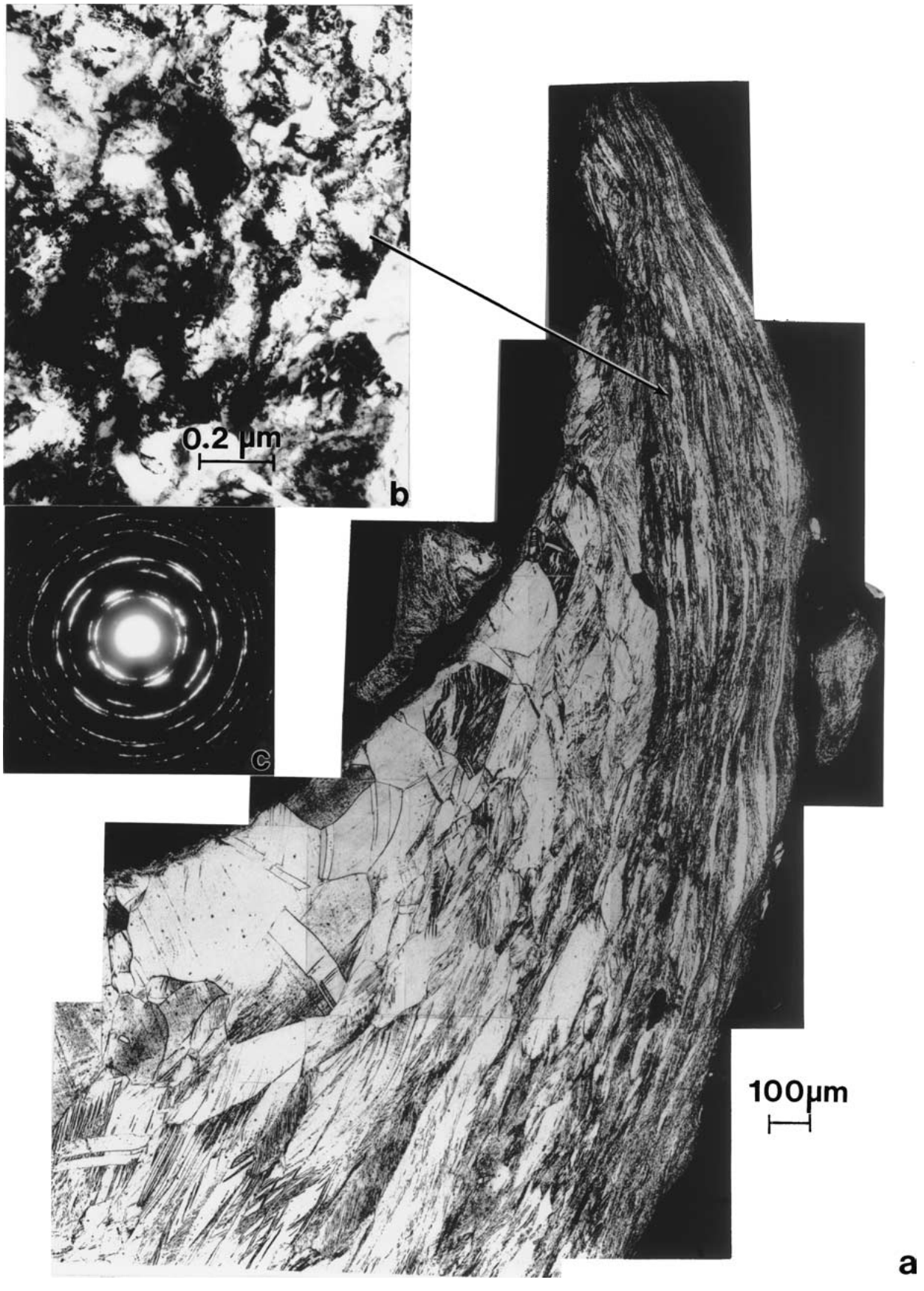

Figure 12 Copper crater rim cross-section showing wide, overlapping shear bands composed of DRX grains shown typically in TEM image (upper left). SAED pattern insert is typical for the DRX regime. Large arrow in upper right shows rim jetting/flow direction out of crater.

mechanism of Jackson [48] as well as the more comprehensive secondary slip-related mechanism of Huang and Gray [18]. In either case, the promotion of some type of cross slip either through a high SFE or a shift to spherical shock with its characteristically unique deviatoric stress as shown schematically in Fig. 10 will facilitate or favor microband formation over microtwin formation.

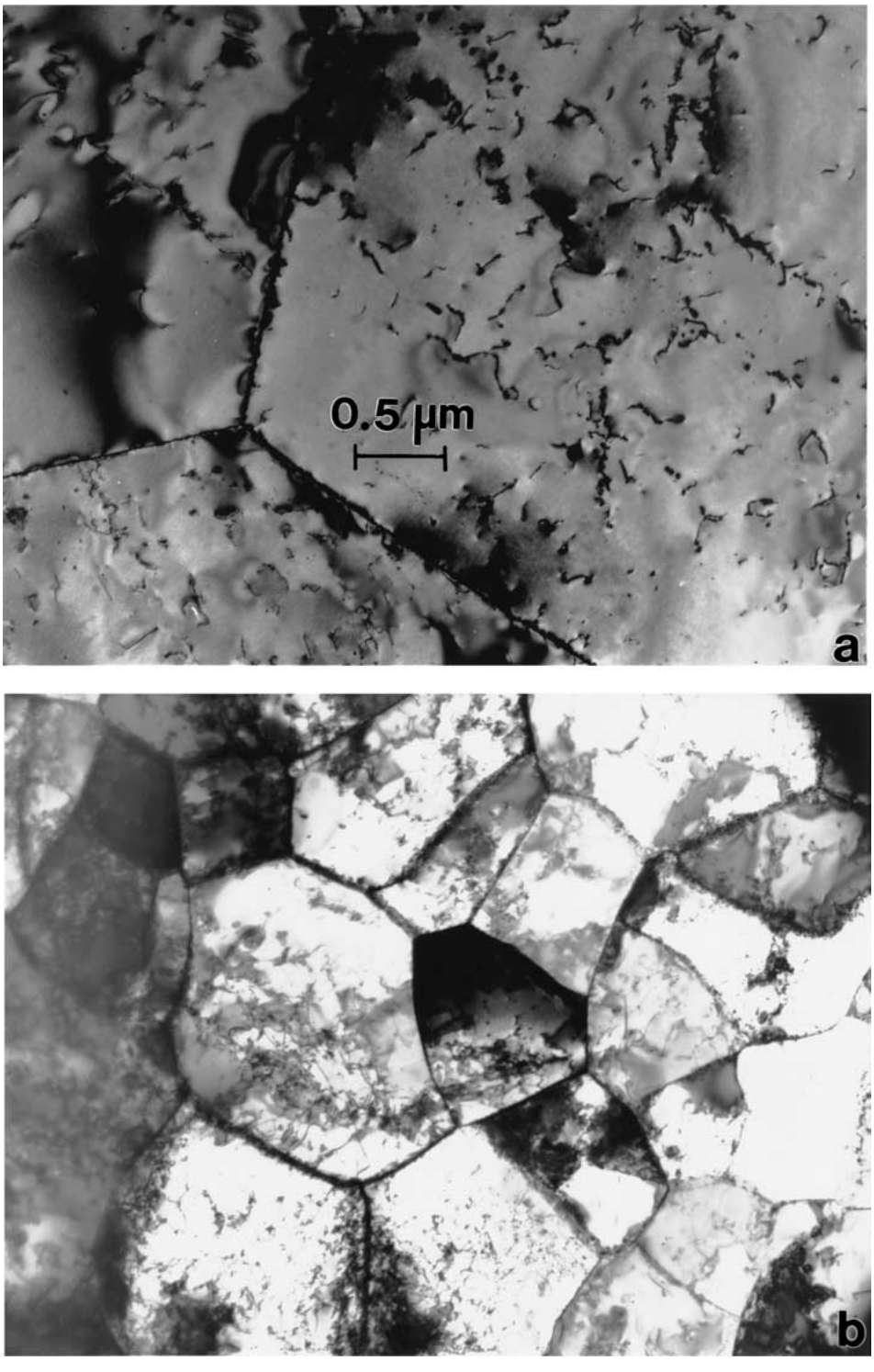

Figure 13 Comparison of starting Ta shaped charge liner microstructure (a) with the DRX microstructure at the center of a recovered Ta shaped charge jet fragment (b). TEM bright-field images. Magnification of (a) and (b) is the same as shown in (a).

3.3. Shear bands, dynamic recrystallization, and solid-state flow at high-strain-rates

Recently Murr *et al*. [55] extensively reviewed and described the role of dynamic recrystallization in facilitating a host of high-strain, high-strain-rate deformation processes involving solid-state flow. Features such as shaped charge jet extension and impact crater formation, especially rim formation and jetting of material from the crater rim [24], involve the formation of various shear instability regimes as a consequence of localized dynamic recrystallization, and the flow facilitated by the fine-grain, recrystallized and often intermixed dynamically recovered material. The creation of shear instabilities through massive, localized dislocation motion was earlier described in a dislocation avalanche model for shear bands by Armstrong *et al*. [56]. In the development of impact craters, for example, a thin (∼50 to 150 μm thick) zone of overlapping, adiabatic shear bands composed of DRX grains allow material to move up the crater wall and form a rim where material is lost by particulation or jetting. Fig. 11 illustrates an impact crater in an Fe target along with a TEM view and SAED pattern insert illustrating the small grain structure composing the DRX zone at the crater wall. Fig. 12

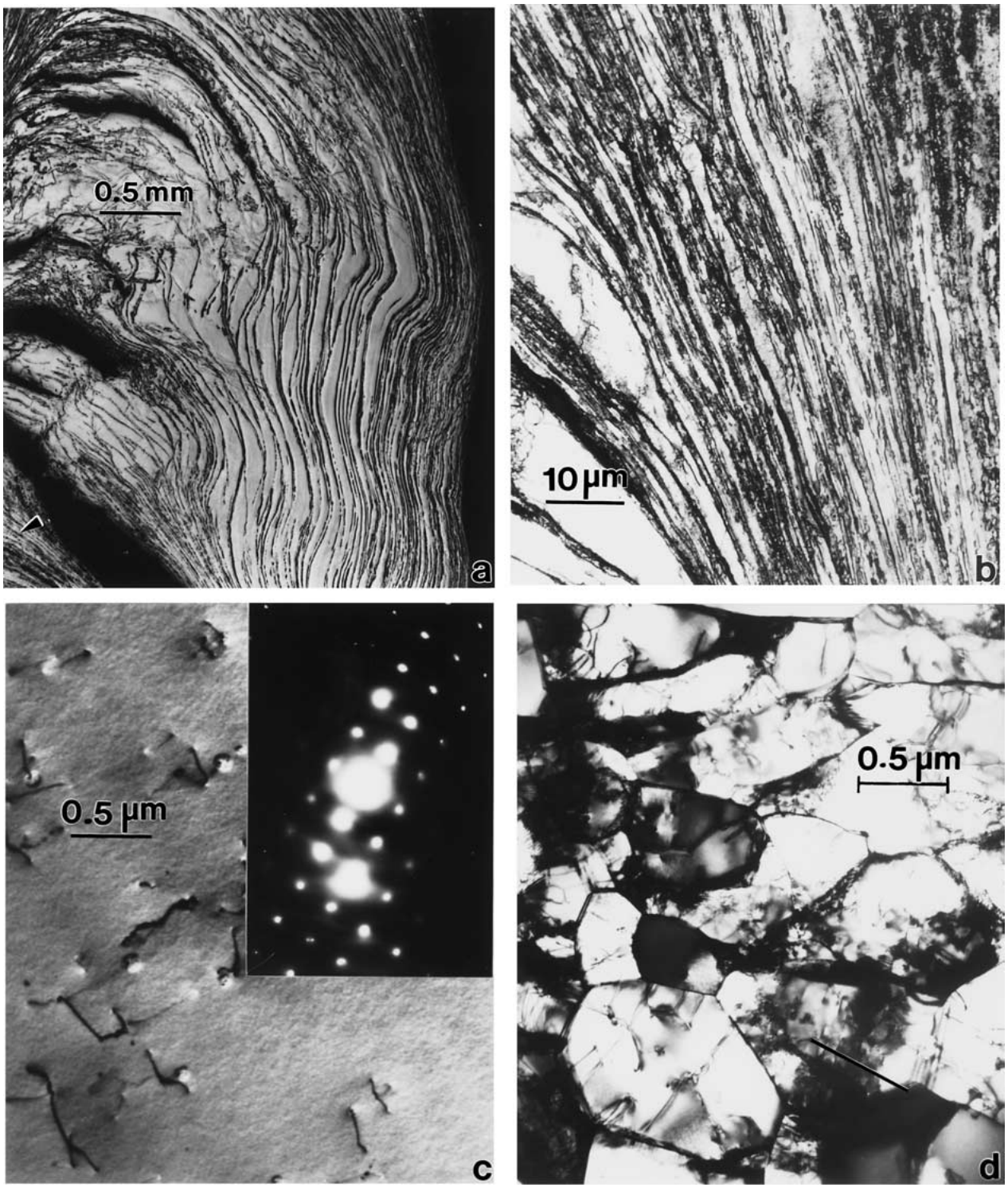

Figure 14 W-4% Ta [001] single-crystal rod penetrator segment in RHA (a). (b) Magnified view showing DRX in shear band flow regime near arrow in (a). (c) TEM image of initial [001] rod section. (d) TEM image typical of DRX and DXV microstructure in (b).

illustrates a more dramatic view of the shear band/DRX regime composing a crater rim in a copper target along with a corresponding TEM image and an SAED pattern exhibiting highly misoriented DRX grains. It can be noted that the microbands created in the microstructure appear to aggregate within the overlapping shear bands and are in effect precursors to the DRX regime. Fig. 13 continues the examples of DRX in extreme deformation at high rates by comparing the starting liner TEM microstructure with the DRX microstructure typical of the center of a recovered Ta shaped charge jet fragment. In the DRX examples shown for Fe, Cu, and Ta in Figs 11–13 the so-called steady-state grain size is <1 μm. Note that the TEM images may exhibit residual (static or dynamic) grain growth which increases the steady-state grain size.

The arrows in Fig. 12 typically illustrate the microbands which form and when the image is perused from left to right the microbands and heavily deformed grains merge with the adiabatic shear/DRX bands at the inside rim edge as noted previously. Dense microtwin zones have been observed to merge with overlapping shear bands/DRX zones in an iron EFP (explosively-formed penetrator) [21] and in a columnar-grain [001]

tungsten rod penetrated into RHA (rolled homogeneous armor). These shear/DRX zones facilitate solid state flow similar to that illustrated for crater rim formation in Fig. 12. Fig. 14a and b illustrate these flow features in a W-4% Ta [001] single-crystal fragment in RHA along with TEM views of the starting [001] section microstructure and the corresponding deformation-flow zone (DRX and DRV) microstructure in Fig. 14c and d respectively. A simple view of flow and counterflow in the penetration of a rod into a metal target (W-4% Ta into Cu for example) can be visualized by effectively placing the image of Fig. 14b in contact with Fig. 12a where flow in both the penetrator and the target are facilitated by overlapping DRX regimes. These DRX regimes often emerge from dense, overlapping microtwin or microband zones which serve as precursors or precursor microstructures. In this regard, there are severe deformation circumstances, such as rim development and flow in impact crater formation illustrated in Fig. 12 where ideally twins, microbands, grain size effects, shear bands, and DRX and DRV are all interrelated.

4. Summary and conclusions

To a large extent this paper represents a rather broad brush review of deformation twinning, particularly shock-induced deformation microtwins in fcc and bcc metals and alloys, microbands associated with impact cratering-related phenomena, grain size effects on microbands and microtwins, adiabatic shear bands, and DRX. The effect of deformation mode, particularly planar shock versus ideal spherical shock in impact cratering on the microtwin-microband transition has been described, and the effect of SFE illustrated. The connection between microbands and microtwins to DRX and especially the development of dense and overlapping adiabatic shear bands in solid-state flow processes has been broadly illustrated.

The comparison of microstructures as they apply to extreme deformation—at high strain and high strain rates—begins to provide a general understanding especially of solid-state flow of metals and alloys. The evolution and progression of dynamic deformation phenomena seems to provide a metaphorical parallel to the dynamics of intellectual pursuit and its role in establishing a basic understanding of rather complex materials phenomena.

Acknowledgments

This research was supported in part by a Mr. and Mrs. MacIntosh Murchison Endowed Chair at the University of Texas at El Paso and by NASA Grants NAG-9-1171 and NAG-9-1100 through the NASA Johnson Space Center, Houston, TX. We are grateful for the contributions of Dr. Fred Hörz at NASA Johnson Space Center in impact crater experiments.

References

1. J. S. RINEHART and J. PEARSON, "Behavior of Metals Under Impulsive Loads" (ASM, Metals Park, OH, 1954).
2. M. H. RICE, R. G. MC QUEEN and J. M. WALSH, "Compression of Solids by Strong Shock Waves, Solid State Physics," Vol. 6 (Academic Press, NY, 1958).
3. C. S. SMITH, *Trans. AIME* **212** (1958) 574.
4. P. W. SHEWMON and V. F. ZACKAY (eds.), "Response of Metals to High-Velocity Deformation" (Wiley-Interscience, NY, 1961).
5. R. W. ARMSTRONG, *J. Mech. Phys. Sol.* **9** (1961) 196.
6. M. W. MEYERS, *Scripta Met.* **12** (1978) 21.
7. W. ARNOLD, Dynamische Werkstoffuervhatten von Armco-Eisen bei Stosswellenbelastung, Fortschr. - Ber. VDl-Verlag, Dusseldorf, Reiche 5, Nr. 247, 1992.
8. K. WONGWIWAT and L. E. MURR, *Mater. Sci. Engr.* **35** (1978) 273.
9. M. A. MEYERS, "Dynamic Behavior of Materials" (Wiley, NY, 1994).
10. R. W. ARMSTRONG and F. J. ZERILLI, in "Fundamental Issues and Applications of Shock-Wave and High-Strain-Rate Phenomena," Chap. 15 edited by K. P. Staudhammer, L. E. Murr and M. A. Meyers (Elsevier Science Ltd., Amsterdam, 2001) p. 115.
11. M. A. MEYERS, U. R. ANDRADE and A. H. CHOKSHI, *Met. and Mater. Trans.* **26A** (1995) 2881.
12. R. W. ARMSTRONG and P. J. WORTHINGTON, in "Metallurgical Effects at High Strain Rates," edited by R. W. Rohde *et al.* (Plenum Press, NY, 1973) p. 401.
13. L. E. MURR, in "Shock Waves in Condensed Matter," edited by S. C. Schmidt and N. C. Holmes (Elsevier Science, Amsterdam, 1988) p. 315.
14. R. J. DE ANGELIS and J. B. COHEN, *J. Metals* **15** (1963) 681.
15. M. A. MEYERS and L. E. MURR, in "Shock Waves and High-Strain-Rate Phenomena in Metals," Chap. 3 edited by M. A. Meyers and L. E. Murr (Plenum Press, New York, 1981) p. 487.
16. S. A. QUINONES, J. M. RIVAS and L. E. MURR, *J. Mater. Sci. Lett.* **14** (1995) 685.
17. S. A. QUINONES and L. E. MURR, *Phys. Stat. Sol.* (a) **166** (1998) 763.
18. J. C. HUANG and G. T. GRAY, III, *Acta Metall.* **37**(2) (1989) 3335.
19. J. C. SANCHEZ, L. E. MURR and K. P. STAUDHAMMER, *Acta Mater.* **45**(8) (1997) 3223.
20. S. PAPPU, S. SEN, L. E. MURR, D. KAPOOR and L. S. MAGNESS, *Mater. Sci. Engng.* A **298** (2001) 144.
21. S. PAPPU and L. E. MURR, *ibid.* A **284** (2000) 148.
22. L. E. MURR, H. K. SHIH and C.-S. NIOU, *Mater. Character.* **33** (1994) 65.
23. L. E. MURR, C.-S. NIOU, J. C. SANCHEZ, H. K. SHIH, L. DU PLESSIS, S. PAPPU and L. ZERNOW, *J. Mater. Sci.* **30** (1995) 2747.
24. L. E. MURR, C.-S. NIOU, E. P. GARCIA, E. FERREYRA, J. M. RIVAS and J. C. SANCHEZ, *Mater. Sci. Engng.* A **222** (1997) 118.
25. L. E. MURR, "Interfacial Phenomena in Metals and Alloys" (Addison-Wesley. Reading, MA, 1975) reprinted by Tech Books (1991) and available through CBLS, 119 Brentwood St., Marietta, OH 45750: FAX 740-374-8029.
26. *Idem.*, in "Shock Waves and High-Strain-Rate Phenomena in Metals," Chap. 37 edited by M. A. Meyers and L. E. Murr (Plenum Press, New York, 1981) p. 607.
27. A. C. GUREVITCH, L. E. MURR, H. K. SHIH, C.-S. NIOU, A. H. ADVANI, D. MANUEL and L. ZERNOW, *Mater. Character.* **30** (1993) 201.
28. H. J. SHIH, L. E. MURR, C.-S. NIOU and L. ZERNOW, *Scripta Met. et Mater.* **29** (1993) 1291.
29. L. E. MURR, J. M. RIVAS, S. QUINNES, C.-S. NIOU, A. H. ADVANI and B. MARQUEZ, *J. Mater. Sci.* **28** (1993) 4553.
30. J. M. RIVAS, L. E. MURR, C.-S. NIOU, A. H. ADVANI and D. J. MANUEL, *Scripta Met. et Mater.* **27** (1992) 919.
31. S. A. QUINONES, J. M. RIVAS, E. P. GARCIA and L. E. MURR, *J. Mater. Sci.* **31** (1996) 3921.
32. W. HUANG, C.-S. NIOU, L. E. MURR, N. L. RUPERT and F. I. GRACE, in "Metallurgical and Materials Applications of Shock-Wave and High-Strain-Rate Phenomena," Chap. 33 edited by

L. E. Murr, K. P. Staudhammer and M. A. Meyers (Elsevier Science, Amsterdam, 1995) p. 265.
33. C. KENNEDY and L. E. MURR, *Mater. Sci. Engng.* A **325** (2002) 131.
34. S. PAPPU, C. KENNEDY, L. E. MURR, L. S. MAGNESS and D. KAPOOR, *ibid.* A **262** (1999) 115.
35. E. A. TRILLO, E. V. ESQUIVEL, L. E. MURR and L. S. MAGNESS, *Mater. Character.* **48** (2002) 407.
36. F. GREULICH and L. E. MURR, *Mater. Sci. Engng.* **39** (1979) 81.
37. L. E. MURR, A. AYALA and C.-S. NIOU, *Ibid.* A **216** (1–2) (1996) 69.
38. L. E. MURR and F. I. GRACE, *Trans. Met. Soc. AIME* **245** (1969) 2225.
39. L. E. MURR, E. A. TRILLO, A. A. BUJANDA and N. E. MARTINEZ, *Acta Mater.* **50** (2002) 121.
40. L. E. MURR, A. A. BUJANDA, E. A. TRILLO and N. E. MARTINEZ, *J. Mater. Sci. Lett.* **21** (2002) 559.
41. L. E. MURR, M. A. MEYERS, C.-S. NIOU, Y. J. CHEN, S. PAPPU and C. KENNEDY, *Acta Mater.* **45**(1) (1997) 157.
42. L. E. MURR, K. P. STAUDHAMMER and S. S. HECKER, *Metal. Trans.* **13**A (1982) 627.
43. K. P. STAUDHAMMER, L. E. MURR and S. S. HECKER, *Acta Met.* **31** (1983) 267.
44. J. B. COHEN and J. WEERTMAN, *ibid.* **11** (1963) 997, 1368.
45. A. W. SLEESWYK, *ibid.* **10** (1962) 803.
46. M. HATHERLY and A. S. MALIN, *Metal Tech.* **6** (1979) 308.
47. A. S. MALIN and M. HATHERLY, *Metal Sci.* **13** (1979) 463.
48. P. J. JACKSON, *Scripta Metall* **17** (1983) 199.
49. G. T. GRAY and P. S. FOLLANSBEE, in "Shock Waves in Condensed Matter," edited by S. C. Schmidt and N. C. Holmes (Elsevier Science, BV, Amsterdam, 1988) p. 339.
50. K. P. STAUDHAMMER, C. E. FRANTZ, S. S. HECKER and L. E. MURR, in "Shock-Wave and High-Strain-Rate Phenomena in Metals," Chap. 7 edited by M. A. Meyers and L. E. Murr (Plenum Press, New York, 1981) p. 91.
51. R. W. ARMSTRONG and F. J. ZERILLI, *J. de Physique, Coll. C3* **49** (1980) C3-259.
52. F. B. FOLEY and S. P. HOWELL, *Trans. AIME* **68** (1923) 891.
53. S. THUILLIER and E. F. RAUCH, *Acta Metall. et Mater.* **42**(6) (1994) 1973.
54. B. GONZALEZ, L. E. MURR, O. L. VALERIO, E. V. ESQUIVEL and H. LOPEZ, *Mater. Character.* **49**(4) (2003) 359.
55. L. E. MURR, E. A. TRILLO, S. PAPPU and C. KENNEDY, *J. Mater. Sci.* **37** (2002) 3337.
56. R. W. ARMSTRONG, C. S. COFFEY and W. L. ELBAN, *Acta Metall.* **30** (1982) 2111.

Received 21 May
and accepted 12 September 2003